

Polarizability, plasmons, and screening in 1T'-MoS₂ with tilted Dirac bands

Antonios Balassis^{1a}, Godfrey Gumbs², and Oleksiy Roslyak¹

¹ *Department of Physics & Engineering Physics, Fordham University,
441 East Fordham Road, Bronx, NY 10458 USA and*

² *Department of Physics and Astronomy, Hunter College of the City
University of New York, 695 Park Avenue, New York, NY 10065, USA*

(Dated: May 10, 2022)

In the presence of an external vertical electric field and strain, it is evident that 1T'-MoS₂ exhibits tilted Dirac bands which are valley-spin-polarized. Additionally, this material experiences a topological phase change between a topological insulator and band insulator for a critical value of the electric field. Using linear response theory, we calculated the polarization function which is in turn employed to obtain the dielectric function. This latter quantity is subsequently utilized in calculations to determine the plasmons dispersion relation, their decay rate and impurity screening corresponding to various levels of doping, the critical applied vertical electric field strengths and the spin-orbit coupling gap in 1T'-MoS₂ with tilted Dirac bands.

I. INTRODUCTION

Massive anisotropic tilted Dirac systems have been gaining an increasing degree of attention among two-dimensional (2D) materials due to their intriguing properties.[1–6] These include their distinctive anisotropic optical response. [2] Materials like graphene and silicene have an isotropic relativistic spectrum in momentum space. [7, 8] However, it has been found that some of these new materials under consideration have anisotropic linear spectra, namely, tilted anisotropic linear Dirac cones, which is the case for 1T'-MoS₂ [1, 2] and 8-*Pmmn* borophene, [9–12] partially hydrogenated graphene [13] as well as transition metal dichalcogenides. [2, 14] In effect, the existence of a tilted cone gives rise to fundamentally different electronic and optical behaviors compared with systems whose cones are not tilted. [15] For example, anisotropic plasmon dispersion was reported in Ref. [16] as well as a unique intervalley damping effect. [17, 18]

These materials are semimetals and have no intrinsic band gap, but a gap can be generated by breaking the symmetry, for example. In the case of graphene, the semimetallic behavior can be changed by breaking the inversion symmetry and the opening of a band gap, as demonstrated in Refs. [19, 20], and which leads to the valley Hall effect. It has been found that in the presence of external vertical electric field, 1T'-MoS₂ presents valley-spin-polarized tilted Dirac bands. Additionally, for a critical value of the electric field, the system undergoes a topological transition between the topological insulator and band insulator phases. We investigate the effects due to the vertical electric field and doping on the anisotropic polarization function, plasmon excitations and their decay rates as well as impurity screening for tilted Dirac bands for 1T'-MoS₂ at T=0 K. These calculations, done using linear response theory, reveal the role played by the combined effect due to spin-orbit coupling, band tilting, and vertical electric field on an important collective property with potential device applications. Our results for 1T'-MoS₂ are compared with 8-*Pmmn* borophene, a polymorph of borophene which has an anisotropic tilted Dirac cone [16], and other monolayer tilted gapped Dirac materials, including α -SnS₂, TaCoTe₂, and TaIrTe₄, based on the similarity of their band structure.

The rest of this paper is organized as follows. For our theory, we introduce in Sec. II a low-energy model Hamiltonian for 1T'-MoS₂. We analytically derive the eigenstates. In Sec. III, we derive the frequency-dependent polarization function and present our numerical results. Section IV is devoted to an investigation of the plasmon excitations and their decay rates for chosen doping and vertical electric field strength. The static shielding of a dilute distribution of impurities is presented in Sec. V. We conclude with a summary in Sec. VI.

II. ANISOTROPIC TILTED DIRAC BANDS FORMALISM

Within the $\mathbf{k} \cdot \mathbf{p}$ approximation the low-energy Hamiltonian for a 2D anisotropic tilted Dirac system representing 1T'-MoS₂ in the vicinity of two independent Dirac points located at $(0, \lambda\Lambda)$ with $\lambda = \pm 1$ is given by [2]

^a Corresponding author: balassis@fordham.edu

$$\hat{\mathcal{H}}_\lambda(k_x, k_y) = \hbar k_x v_1 \gamma_1 + \hbar k_y (v_2 \gamma_0 - \lambda v_- \mathbf{I} - \lambda v_+ \gamma_2) + \Delta(\lambda \gamma_0 - i \alpha \gamma_1 \gamma_2). \quad (1)$$

In this notation, the 2D wave vector $\mathbf{k} = (k_x, k_y)$, the spin-orbit coupling parameter $\Delta = 0.042$ eV and the Fermi velocities are given by $v_1 = 3.87 \times 10^5$ m/s, $v_2 = 0.46 \times 10^5$ m/s, $v_- = 2.86 \times 10^5$ m/s, and $v_+ = 7.21 \times 10^5$ m/s. Also, \mathbf{I} is the unit 4×4 matrix and we have introduced $\gamma_0 = \tau_1 \otimes \sigma_1$, $\gamma_1 = \tau_2 \otimes \sigma_0$, and $\gamma_2 = \tau_3 \otimes \sigma_0$ with, τ_0 and τ_i being unit and Pauli matrices acting in pseudospin space whereas γ_0 and γ_i denote Pauli matrices acting upon real spin space. The normalized electric field $\alpha = |E_z|/|E_c|$ is defined via the applied electric field E_z and its critical value E_c .

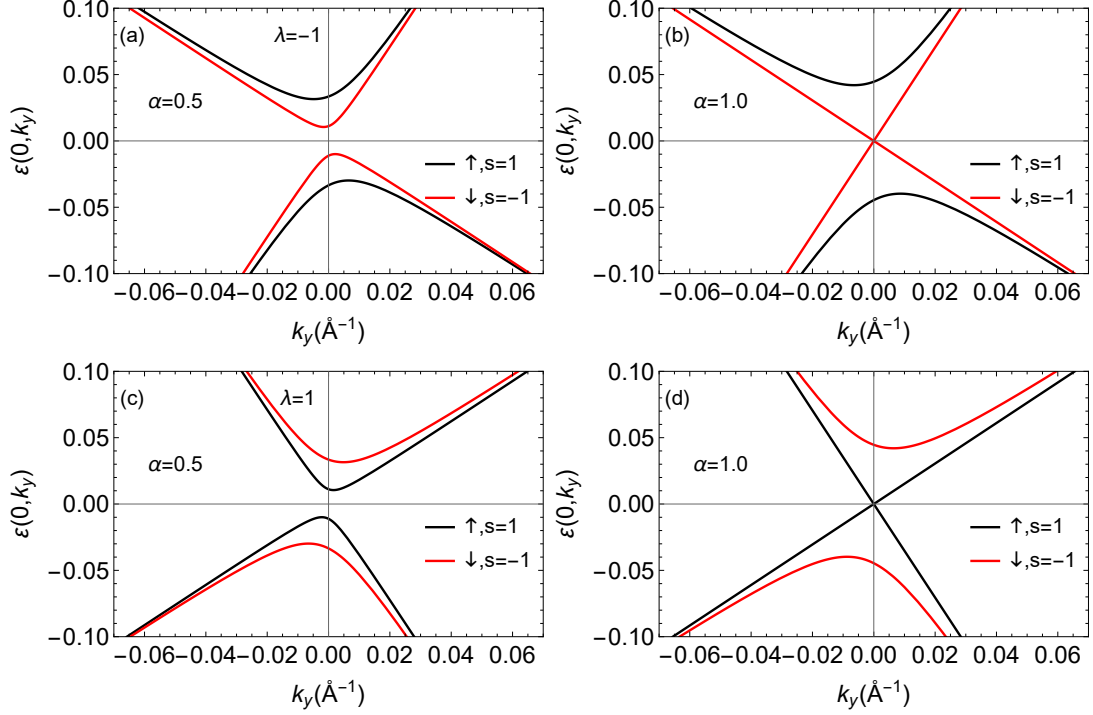


FIG. 1. (Color online) Anisotropic tilted energy bands at the $(0, \lambda)$ points for $\alpha = 0.5$ and $\alpha = 1.0$ when $k_x = 0$. The unit for the energy, is $\hbar k_y v_- = 1.88$ eV ($k_y = 1 \text{ \AA}^{-1}$). Panels (a) and (b) are for $\lambda = -1$, panels (c) and (d) are for $\lambda = 1$.

The energy eigenvalues of Eq. (1) are given by

$$\epsilon_{\xi,s}^\lambda(\mathbf{k}) = -\lambda \hbar v_- k_y + \xi \sqrt{[\hbar v_2 k_y + (\lambda - s\alpha) \Delta]^2 + (\hbar v_1 k_x)^2 + (\hbar v_+ k_y)^2}, \quad (2)$$

where $\xi = \pm 1$ for the conduction (valence) band, and $s = \pm 1$ is the spin up (down) index. The long wavelength expansion of the energy eigenvalues for applied electric field not close to its critical value, $\alpha \neq 1$, is

$$\epsilon_{\xi,s}^\lambda(\mathbf{k}) = \xi |\lambda - s\alpha| \Delta + \{-\lambda \hbar v_- + \xi \hbar v_2 \text{sgn}(\lambda - s\alpha)\} k_y + \left(\frac{\xi \hbar^2}{2\Delta |\lambda - s\alpha|} \right) (v_1^2 k_x^2 + v_+^2 k_y^2), \quad (3)$$

and we see that it depends on both k_y (a linear term) and k_y^2 but only on a k_x^2 quadratic term. Equation (3) also shows that the spin-orbit coupling opens up a gap between spin-subbands and between the valence and conduction bands within a chosen valley. We emphasize that Eq. (3) is not valid in the gapless case.

In Fig. 1, we show the spin-polarized bands and the valley-spin polarized gaps in the presence of a vertical electric field ($\alpha \neq 0$). Notice that an indirect energy gap opens when $\alpha \neq 1$. The critical points of the energy bands are

located at $\mathbf{k}^* = (0, \kappa(s, \xi, \lambda))$ whose coordinate on the k_y -axis for the minima (for $\xi = 1$) or maxima (for $\xi = -1$) of Eq. (2) are

$$\kappa(s, \xi, \lambda) = \frac{\left(\xi v_+ v_- - v_2 \sqrt{v_2^2 - v_-^2 + v_+^2} \right) (\lambda - s\alpha) \Delta}{\hbar (v_2^2 + v_+^2) \sqrt{v_2^2 - v_-^2 + v_+^2}}. \quad (4)$$

According to Eq. (4), the critical point is at the origin when $\lambda = s\alpha$ which is in agreement with the panels on the right-hand side in Fig. 1 for both spin branches and valleys. We now have an explicit expression for the shifted critical point as well as the tilt by taking the gradient of the expression in Eq. (3).

The wave functions of the Hamiltonian in Eq. (1) are given by the following expression

$$\psi_{\xi,s}^\lambda(\mathbf{k}, \mathbf{r}) = \begin{pmatrix} \frac{-\lambda \hbar k_y v_+ + \xi \sqrt{|G|^2 + (\hbar k_y v_+)^2}}{G} \\ \frac{\lambda \hbar k_y v_+ - \xi \sqrt{|G|^2 + (\hbar k_y v_+)^2}}{sG} \\ -s \\ 1 \end{pmatrix} \frac{e^{i\mathbf{k} \cdot \mathbf{r}}}{\sqrt{A}}, \quad (5)$$

where A is a normalization area and we have introduced $G \equiv (\lambda - s\alpha)\Delta + \hbar v_2 k_y - i s \hbar v_1 k_x$.

III. FREQUENCY-DEPENDENT POLARIZATION FUNCTION

In the RPA, the polarizability is represented by a particle-hole bubble in the Feynman diagram representation. Mathematically, this is for each channel

$$\Pi_\lambda(\mathbf{q}, \omega) = \sum_{\xi,s} \sum_{\xi',s'} \int \frac{d^2\mathbf{k}}{(2\pi)^2} \frac{f(\epsilon_{\xi',s'}^\lambda(\mathbf{k} + \mathbf{q})) - f(\epsilon_{\xi,s}^\lambda(\mathbf{k}))}{\hbar\omega + \epsilon_{\xi',s'}^\lambda(\mathbf{k} + \mathbf{q}) - \epsilon_{\xi,s}^\lambda(\mathbf{k}) + i\delta} F_{\xi,s,\xi',s'}^\lambda(\mathbf{k}, \mathbf{q}), \quad (6)$$

where $f(\epsilon_{\xi,s}^\lambda(\mathbf{k}))$ is the Fermi-Dirac distribution function under chemical potential μ and $\epsilon_{\xi,s}^\lambda(\mathbf{k})$ are the energy eigenvalues, $\delta = 0^+$ can be viewed as an infinitesimal scattering rate. The numerator containing the two statistical functions ensures that the integrand covers only the overlap of particle-hole pairs $|\lambda, \xi, s, \mathbf{k} \rangle$ and $|\lambda, \xi', s', \mathbf{k} + \mathbf{q} \rangle$ (as opposed to particle-particle or hole-hole pairs). The definition of the overlap function $F_{\xi,s,\xi',s'}^\lambda(\mathbf{k}, \mathbf{q})$ is

$$F_{\xi,s,\xi',s'}^\lambda(\mathbf{k}, \mathbf{q}) \equiv |\langle \psi_{\xi,s}^\lambda(\mathbf{k}) | \psi_{\xi',s'}^\lambda(\mathbf{k} + \mathbf{q}) \rangle|^2. \quad (7)$$

The parameters used in our calculations are the same as before. In Fig. 2, we present the static polarization function versus wave number at zero temperature for various chemical potentials, chosen $\alpha = 0.5$ and 1.0 . We have included the contributions to the polarizability from both valleys, i.e., $\lambda = \pm 1$. More explicitly, in Figs. 2(a) and 2(b), we set $\lambda = \pm 1$ in the sum in Eq. (6) and compare the total value of the polarization function as the chemical potential is varied in Fig. 2(a) whereas Fig. 2(b) shows the individual contributions from the valence (VB) and the conduction (CB) to the total polarizability. These results show that the value of the polarization is increased as the chemical potential is increased but its variation with q_y is not monotonic. Figure 2(b) shows that the contribution to the polarizability is dominated by the conduction band (CB) at longer wavelengths but the valence band (VB) makes the larger contribution as q_y is increased. Our calculations show that the behaviors of the polarizability when $\alpha = 1.0$ are essentially the same as those for $\alpha = 0.5$ in Figs. 2(a) and 2(b). However, we note that at large q_y and high chemical potential, the behavior of the plots is basically linear as it is for monolayer graphene.[21–25]

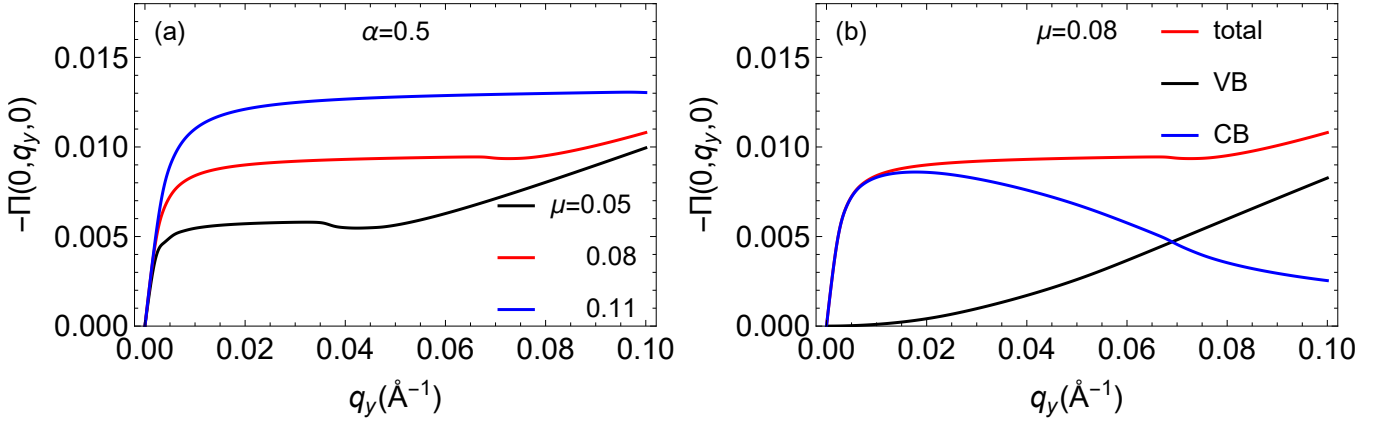


FIG. 2. (Color online) (a) Static polarization using the $\lambda = \pm 1$ energy bands of Fig. 1 for $\alpha = 0.5$ and various values of the chemical potential μ in the conduction band. The chemical potential has the same unit as the energy, (b) Contributions from the valence band (VB) and from the conduction band (CB) to the total polarization for $\mu = 0.083$.

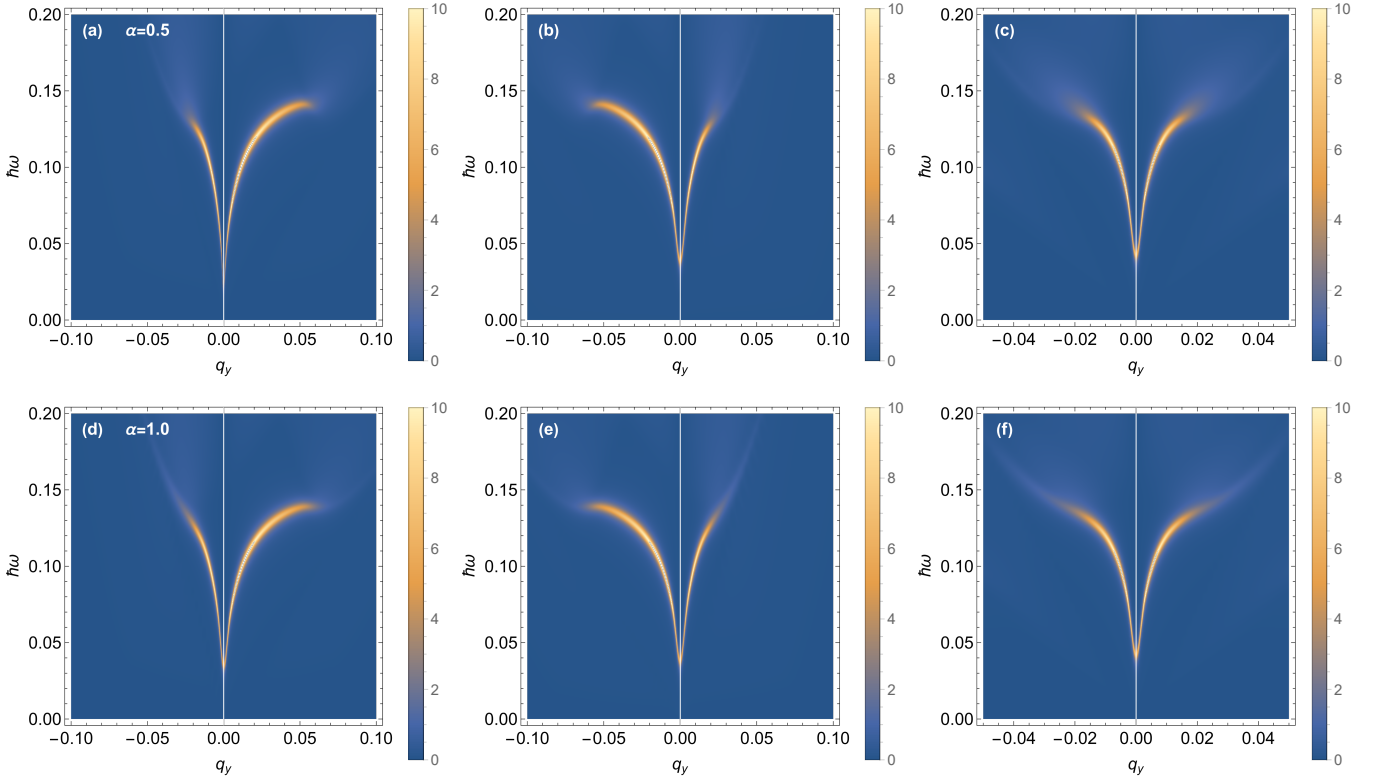


FIG. 3. (Color online) Plasmon dispersion along the q_y direction when $\mu = 0.1$. For the panels in the first row, $\alpha = 0.5$ and $\lambda = -1$ in (a), $\lambda = 1$ in (b) and the sum over both valleys $\lambda = \pm 1$ in (c). In the second-row panels, we chose $\alpha = 1.0$ for the same values of λ as the first row.

IV. ANISOTROPIC PLASMON MODES

The energy dispersion for the self-sustained plasmon oscillations is determined by the zeros of the dielectric function, $\varepsilon(\mathbf{q}, \omega_p - i\gamma) = 0$, where $\varepsilon(\mathbf{q}, \omega) = 1 - v(q) \sum_{\lambda} \Pi_{\lambda}(\mathbf{q}, \omega)$, with $v(q) = e^2/2\varepsilon_0 q$ and the plasmon decay rate is

$$\gamma(\mathbf{q}, \omega_p) = - \frac{\text{Im } \Pi(\mathbf{q}, \omega_p)}{\partial \text{Re } \Pi(\mathbf{q}, \omega) / \partial \omega_p} . \quad (8)$$

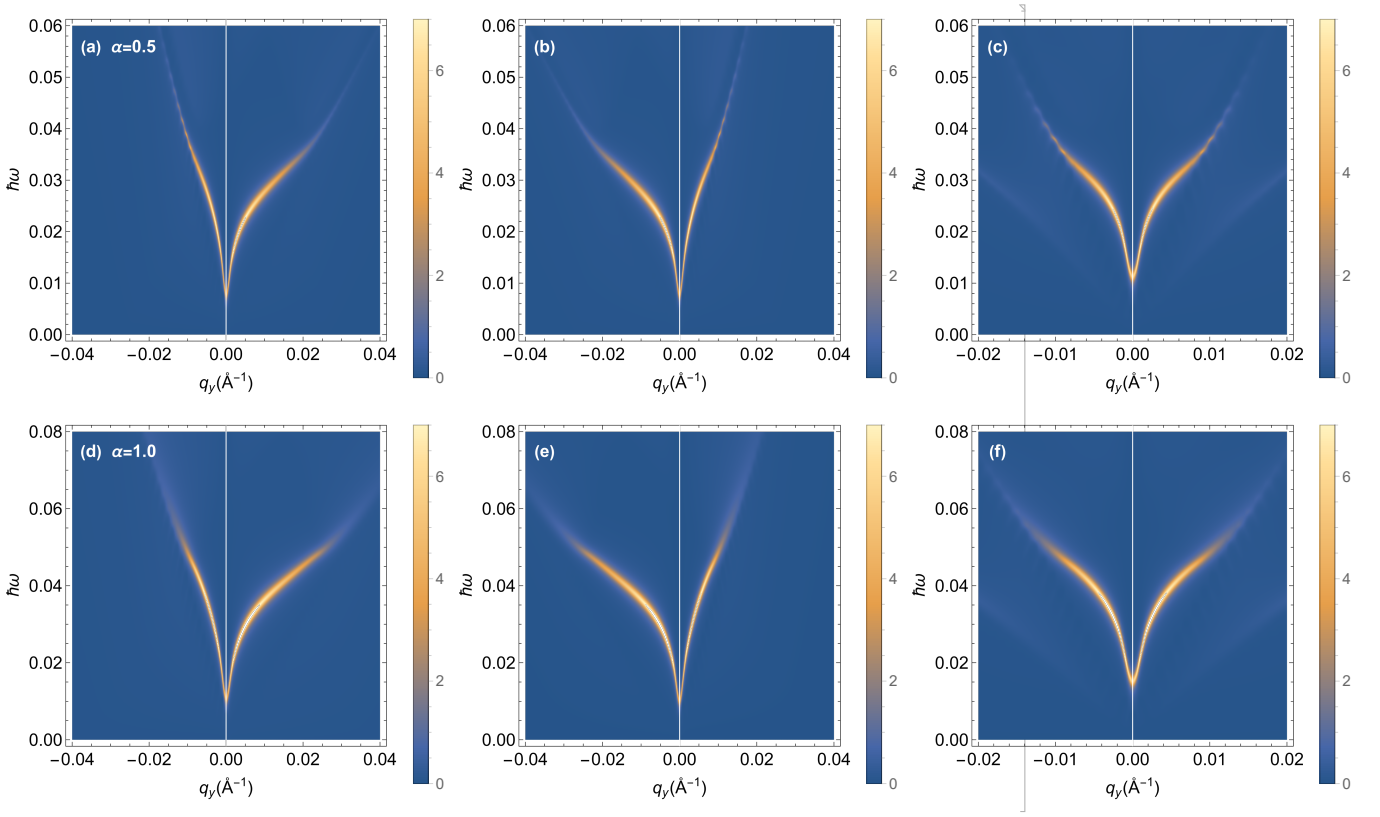


FIG. 4. (Color online) Plasmon dispersion along the q_y direction. In the first row panels, $\alpha = 0.5$, $\mu = 0.03$ (just below the minimum of the higher conduction subband) and $\lambda = -1$ in (a), $\lambda = 1$ in (b) and the sum over both valleys $\lambda = \pm 1$ in (c). In the second row-panels we chose $\alpha = 1.0$, $\mu = 0.04$ (just below the minimum of the higher conduction subband) for the same values of λ correspondingly as the first row.

In Fig. 3, we present the plasmon dispersion for $\alpha = 0.5, 1.0$, $\mu = 0.1$ whereas in Fig. 4, we present the plasmon dispersion for $\alpha = 0.5$, $\mu = 0.03$ and $\alpha = 1.0$, $\mu = 0.04$. In the former case, the chemical potential crosses both conduction subbands whereas in the latter case, the chemical potential falls just below the minimum of the higher of the two conduction subbands. These results illustrate the anisotropy of the dispersion for both chosen values of α , i.e., the plasma frequency depends on the direction of propagation. In all cases, the plasmon modes are Landau damped beyond a critical value of the wave vector q_y which varies with μ and α . As this Landau damping takes place within the particle-hole continuum, we are principally interested in the plasmon branch in the region outside this continuum, where $\text{Im}\Pi = 0$ which yields $\gamma = 0$. The presented results also illustrate that the two valleys contribute unequally. Comparing Figs. 3 and 4, we see that the larger α has a greater group velocity in the long wavelength limit, thereby accounting for the collective properties of tilted MoS_2 .

In Fig. 5, we present the plasmon dispersion for $\alpha = 0.5$, $\mu = 0.1$ where the plasmons isofrequency contours are shown when we sum over both valleys but intervalley terms are not included. Both panels on the left and middle shown in Fig. 5 (a) clearly illustrate the anisotropy of the plasmon dispersion is due to both valleys. Figure 5 demonstrates that the breaking of the symmetry by the electric field leads to a dependence on the direction of propagation of the modes. Choosing a frequency of oscillations in Fig. 5 shows that this value can be achieved in various directions of propagation.

Figure 6 shows the plasmon excitations and corresponding decay rates when $\alpha = 0.5$ and $\alpha = 1.0$. In Fig. 6(a), the chemical potential is $\mu = 0.1$ located in the higher conduction subband so that both conduction subbands are partially occupied. However, in Fig. 6(b), the chemical potential is $\mu = 0.04$ located below the higher conduction subband so that only one conduction sub-bands is partially occupied. The decay rate outside the particle hole region seems enhanced in Fig. 6 shows the plasmon excitations and corresponding decay rates when $\alpha = 0.5$. In Fig. 6 (a) for the higher chemical potential thereby indicating the tunability of γ for $1\text{T}'\text{-MoS}_2$.

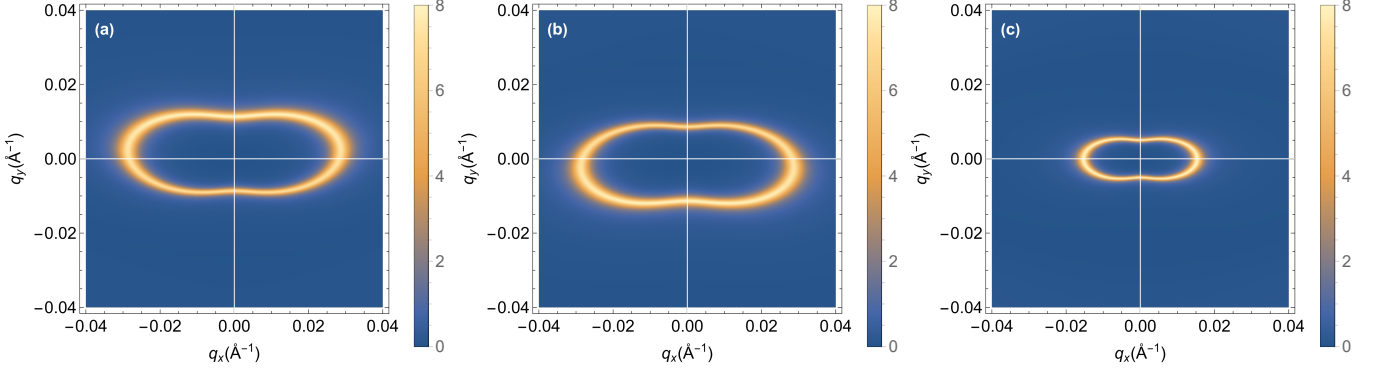


FIG. 5. (Color online) Plasmon isoenergy plot for $\alpha = 0.5$, $\mu = 0.1$ when (a) $\lambda = -1$, (b) $\lambda = 1$ and (c) when we sum over both valleys $\lambda = \pm 1$.

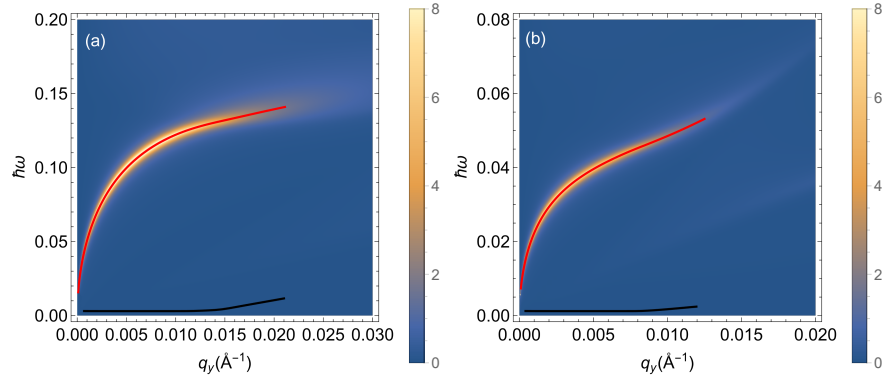


FIG. 6. (Color online) Decay rate γ (lower black curve) of the plasmon (upper red curve) versus q_y for (a) $\alpha = 0.5$, $\mu = 0.1$ and (b) $\alpha = 1.0$, $\mu = 0.04$ when both valleys contribute to the polarization. In (a), the chemical potential is located in the upper conduction sub-band (both conduction sub-bands are partially filled). In (b), the chemical potential is located under the bottom of the higher conduction sub-band (only the lowest conduction subband is occupied). The unit for γ is the same as the energy unit used before for the plasmon dispersion, $\hbar q_y v_-$ with $q_y = 1 \text{ \AA}^{-1}$.

V. STATIC SCREENING EFFECTS

We now employ the static limit of the polarizability $\Pi(\mathbf{q}, \omega = 0)$ or Lindhard function to calculate the screened Coulomb potential. This means that from the Lindhard function, it is possible to obtain the response of the Dirac fermions in the material to the presence of a magnetic or electric impurity. The potential in the vicinity of a point charge Q is proportional to the Fourier transform of the screened Coulomb interaction

$$\Phi(\mathbf{r}) = \frac{Q}{\epsilon_0} \int \frac{d^2 \mathbf{q}}{(2\pi)^2} \frac{v(\mathbf{q})}{\epsilon(\mathbf{q})} e^{i\mathbf{q} \cdot \mathbf{r}}, \quad (9)$$

where $\epsilon(\mathbf{q}) = \epsilon(\mathbf{q}, \omega = 0)$ and since the Lindhard function is anisotropic in \mathbf{q} -space, we must take into consideration its dependence on the polar angle of integration in Eq. (9).

In Fig. 7, we present the static screened potential for a dilute distribution of charge for which Eq. (9) is applicable. The calculated results show evidence of anisotropy along the mutually perpendicular x and y axes. The screened potential displays Friedel oscillations with directional dependent amplitudes which are phase shifted. This is quite unlike the screened electrostatic potential for graphene and the difference is attributed to the significant variation in their band structures.

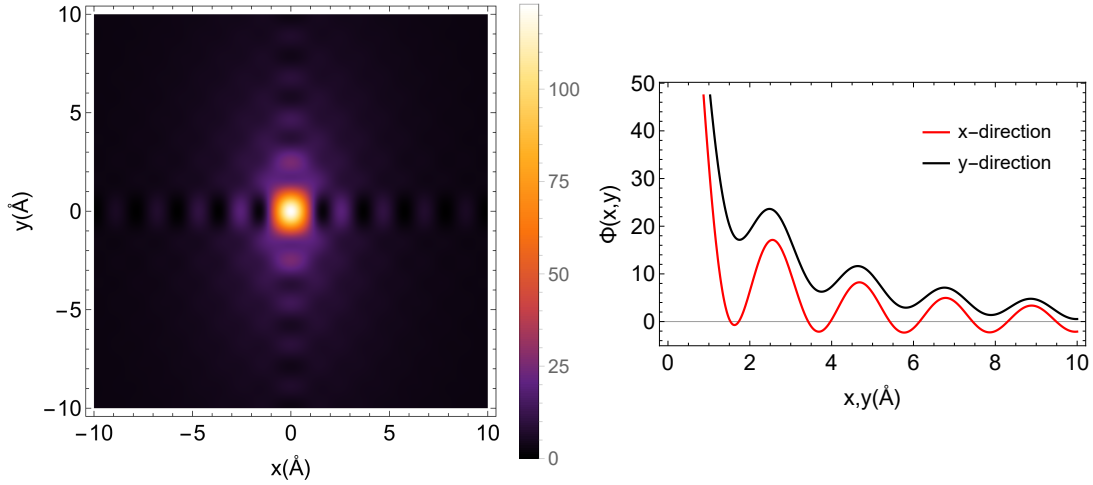


FIG. 7. (Color online) Screened potential $\Phi(x, y)$ for $\alpha = 0.5$, $\mu = 0.1$ with both valleys included in the dielectric function. In the left panel, we present a density plot for different distances x, y from the screened charge Q . In the right panel, we see the variation of the potential in units of $48.1Q/\epsilon_0\text{\AA}$ along the x and y directions.

VI. CONCLUDING REMARKS

In conclusion, we have investigated the behavior of the dynamical polarizability, plasmon excitations as well as the static shielding of a dilute distribution of charged impurities for 1T'-MoS₂ in the presence of an external vertical electric field and strain. We also demonstrated that the plasmon damping rate generally increases for larger wavevector q_y and larger frequencies along a plasmon branch. Therefore, we expect our damping rate to be monotonically increasing with q_y . The tilted Dirac bands which are valley-spin-polarized cause this material to undergo a topological phase change between a topological insulator and band insulator corresponding to a critical value of the electric field. We employed linear response theory to calculate the polarization function which was obtained numerically at T=0 K. These results were then substituted into the dielectric function for calculating the plasmon dispersion relation, their decay rate and impurity screening. We would like to once again emphasize that here we have calculated both damped and undamped plasmons as zeros of the real part of the dielectric function.

Such distinctive features of 1T'-MoS₂ are expected to give rise to a variety of applications which can be used for designing novel multi-functional nanoelectronic and nanoplasmonic devices. Specifically, the control of these collective properties could lead to some important technological applications for electronic and optoelectronic devices.

It is evident that the electron dynamics in 1T'-MoS₂ under a vertical electric field and strain is significantly different from that in graphene and this variation can be controlled by an electrostatic potential. This further implies that such a difference may be tuned by a structure parameter α for 1T'-MoS₂. These results presented here are expected to provide very useful information as well as guidance for designing nanoelectronic and nanoplasmonic devices based on innovative low-dimensional 1T'-MoS₂ materials

Finally, we observe that the presence of anisotropic plasmons in 1T'-MoS₂ like in 8-*Pmmn* borophene makes it possible for its use for anisotropic plasma-wave photodetection, in a field-effect transistor-based device.

ACKNOWLEDGMENT(S)

G.G. would like to acknowledge the support from the Air Force Research Laboratory (AFRL) through Grant No. FA9453-21-1-0046

-
- [1] X. Qian, J. Liu, L. Fu, and J. Li, *Science* **346**, 1344 (2014).
 - [2] C.-Y. Tan, C.-X. Yan, Y.-H. Zhao, H. Guo, H.-R. Chang, *et al.*, *Physical Review B* **103**, 125425 (2021).

- [3] M. Mojarro, R. Carrillo-Bastos, and J. A. Maytorena, *Physical Review B* **103**, 165415 (2021).
- [4] R. Ng, A. Wild, M. Portnoi, and R. Hartmann, arXiv preprint arXiv:2111.10760 (2021).
- [5] C.-Y. Tan, J.-T. Hou, C.-X. Yan, H. Guo, and H.-R. Chang, arXiv preprint arXiv:2112.09392 (2021).
- [6] F. Qi and X. Zhou, *Chinese Physics B* (2021).
- [7] T. O. Wehling, A. M. Black-Schaffer, and A. V. Balatsky, *Advances in Physics* **63**, 1 (2014).
- [8] J. Wang, S. Deng, Z. Liu, and Z. Liu, *National Science Review* **2**, 22 (2015).
- [9] M. Nakhaee, S. Ketabi, and F. Peeters, *Physical Review B* **97**, 125424 (2018).
- [10] L.-C. Xu, A. Du, and L. Kou, *Physical Chemistry Chemical Physics* **18**, 27284 (2016).
- [11] A. Lopez-Bezanilla and P. B. Littlewood, *Physical Review B* **93**, 241405 (2016).
- [12] X.-F. Zhou, X. Dong, A. R. Oganov, Q. Zhu, Y. Tian, and H.-T. Wang, *Physical Review Letters* **112**, 085502 (2014).
- [13] H.-Y. Lu, A. S. Cuamba, S.-Y. Lin, L. Hao, R. Wang, H. Li, Y. Zhao, and C. Ting, *Physical Review B* **94**, 195423 (2016).
- [14] X. Qian, J. Liu, L. Fu, and J. Li, *Science* **346**, 1344 (2014).
- [15] Z.-K. Yang, J.-R. Wang, and G.-Z. Liu, *Physical Review B* **98**, 195123 (2018).
- [16] K. Sathukhan and A. Agarwal, *Physical Review B* **96**, 035410 (2017).
- [17] S. F. Islam and A. Jayannavar, *Physical Review B* **96**, 235405 (2017).
- [18] J. Sári, C. Töke, and M. O. Goerbig, *Physical Review B* **90**, 155446 (2014).
- [19] A. Iurov, G. Gumbs, and D. Huang, *Physical Review B* **99**, 205135 (2019).
- [20] A. Iurov, L. Zhemchuzhna, D. Dahal, G. Gumbs, and D. Huang, *Physical Review B* **101**, 035129 (2020).
- [21] G. Gumbs, A. Balassis, D. Dahal, and M. Lawrence Glasser, *The European Physical Journal B* **89**, 1 (2016).
- [22] R. Roldán, J.-N. Fuchs, and M. Goerbig, *Physical Review B* **80**, 085408 (2009).
- [23] R. Roldán, M. Goerbig, and J. Fuchs, *Semiconductor science and technology* **25**, 034005 (2010).
- [24] E. Hwang and S. D. Sarma, *Physical Review B* **75**, 205418 (2007).
- [25] D. K. Patel, S. S. Ashraf, and A. C. Sharma, *Physica Status Solidi (b)* **252**, 1817 (2015).